Compression waves in semi-circular channel

Soechiarto, Emelia Dara; Wuthrich, Davide; Chanson, Hubert

DOI
10.1680/jwama.21.00022

Publication date
2021

Document Version
Accepted author manuscript

Published in
Proceedings of the Institution of Civil Engineers: Water Management

Citation (APA)
Soechiarto, E. D., Wuthrich, D., & Chanson, H. (2021). Compression waves in semi-circular channel. *Proceedings of the Institution of Civil Engineers: Water Management*, *175*(5), 247-256. https://doi.org/10.1680/jwama.21.00022

Accepted manuscript doi:
10.1680/jwama.21.00022

Accepted manuscript doi:
10.1680/jwama.21.00022

Submitted: 26 May 2021

Published online in 'accepted manuscript' format: 27 May 2021

Manuscript title: Compression waves in semi-circular channel

Authors: Emelia Dara Soechiarto[1], Davide Wűthrich[2] and Hubert Chanson[1]

Affiliations: [1]School of Civil Engineering, The University of Queensland, Brisbane QLD, Australia and [2]Department of Hydraulic Engineering, Delft University of Technology, CN Delft, The Netherlands; formarly School of Civil Engineering, The University of Queensland, Brisbane QLD, Australia

Corresponding author: Hubert Chanson, School of Civil Engineering, The University of Queensland, Brisbane QLD 4072, Australia.

E-mail: h.chanson@uq.edu.au

Accepted manuscript doi:
10.1680/jwama.21.00022

Abstract

Partially-filled pipe flows are commonly observed in urban hydraulics, sewers and road crossings. The occurrence of a compression wave in the confined space may result from flash flooding, transient operation or accidental blockage, inducing explosive conditions. In this study, the propagation of a compression wave was studied in a relatively large-size laboratory flume with a semi-circular cross-section. The unsteady flow properties were recorded to understand how the circular cross-sectional shape impacted onto the surging water propagation. Both free-surface and velocity data indicated a marked impact of the compression wave passage, with large instantaneous fluctuations comparable and sometimes larger than observations of compression waves in rectangular channels.

Keywords: Waterways & canals; Hydraulics & hydrodynamics; Sewers & drains

Accepted manuscript doi:
10.1680/jwama.21.00022

Introduction

Open channel flows in circular conduits commonly occur in culverts, sewers, stormwater drains, and hydro-power tunnels (Hager 1999, Sterling and Knight 2000) (Fig. 1A). Similarly, semi-circular flumes are common occurrence in water supply and irrigation systems (Repogle and Chow 1966). The circular shape is extremely simple, yet it is a difficult shape for open channel flow analyses because the cross sectional shape continually varies with increasing flow depth (Kazemipour 1979, Sterling 1998) (Fig. 1B). Figure 1B illustrates the variation in free-surface width B, cross-section area A, wetted perimeter P_w and hydraulic diameter D_H with increasing water depth d, with R the circular open channel radius (Fig. 1C). During some transient conditions in open channels, a sudden rise in water level is called a compression wave (Favre 1935, Treske 1994). The surging waters may induce large transient turbulent stresses, linked to intense turbulent mixing and strong sedimentary transport (Khezri and Chanson 2012, Furgerot et al. 2016). In partially-filled pipes, the propagation of a compression wave can further create explosive conditions, in particular when the free-surface flow quasi-instantly transitions into a pressurised pipe flow (Capart et al. 1997, Pozos et al. 2015). Such an explosive transition was recently recorded in Belo Horizonte, Brazil, in January 2020: during a flash flood induced by heavy rains. The Arrudas River surged in its covered conduit, and burst through the obvert, with geysers jetting out of manholes and road collapses. Several studies investigated one-dimensional unsteady flows in storm sewers, with a focus on the transition from free-surface to pressurised flow (e.g. Cunge and Wegner 1964, Song et al. 1983, Capart et al. 1997). But, the transient turbulence during the compression wave propagation in circular pipes was not studied to date.

The motivation of the present study is to characterise the unsteady turbulent characteristics of surging waters in a semi-circular channel, through some laboratory experiments in a relatively large flume (Fig. 2). The aim is to gain some understanding on how the sudden change in cross-sectional shape in circular conduits may impact, or not, onto the compression wave propagation and transient characteristics.

2. Physical facility and metrology

The laboratory experiments were conducted in a semi-circular channel in the AEB Hydraulic laboratory at the University of Queensland. The bed slope was horizontal for all experiments. The test section was 13.25 m long, with a semi-circular PVC invert with a 0.5 m diameter and vertical glass walls above (Fig. 2). A smooth transition section was installed between x = 0.11 m and x = 1.23 m at the upstream end, while the semi-circular section ended with an abrupt drop and expansion into a 0.5 m wide rectangular section, where x is the longitudinal coordinate measured from the upstream end of the flume.

In steady flows, the water elevations and longitudinal velocities were respectively measured with a pointer gauge and a Prandtl-Pitot tube (Ø = 3.3 mm). During the compression wave experiments, the water depth measurements were performed with five ultrasonic sensors Microsonic^{TM} Mic+25, located along the channel centreline above the flume. The centreline velocities were recorded with an acoustic Doppler velocimeter (ADV) Nortek^{TM} Vectrino+ positioned at x = 7.15 m and y = 0.25 m for several vertical elevations. The ultrasonic sensors and ADV unit were sampled continuously, simultaneously and synchronously, within 1 ms, at 200 Hz for the full duration of each run. The velocimeters were positioned with a fine adjustment travelling mechanism connected to a HAFCO^{TM} digital scale unit, with an error on the vertical position $\Delta z < \pm 0.025$ mm. The error on the longitudinal and transverse position was $\Delta x < \pm 2$ mm and $\Delta y < 1$ mm respectively.

Accepted manuscript doi:
10.1680/jwama.21.00022

The compression waves were generated by the rapid closure of a Tainter gate with a semi-circular shape located at x = 14.0 m. The closure of the gate took place in less than 0.3 s and had no impact on the compression wave propagation. Once generated, the compression wave advanced upstream against an initially-steady free-surface flow (Fig. 2). All recordings ended when the surging waters reached the upstream end of the flume. All the unsteady flow measurements were repeated 25 times, and the ensemble statistics of the data set were calculated. Tables 1 and 2 summarise the flow conditions for the steady flow and compression wave experiments respectively.

3. Steady flow characteristics

The steady flow properties in the semi-circular channel were measured for flow rates between 0.005 m^3/s and 0.080 m^3/s (Table 1). For all discharges, the flow was subcritical, i.e. $d > d_c$ with d_c the critical depth, and the flow depth d decreased with increasing longitudinal distance. That is, the longitudinal free-surface data showed a H2 backwater profile for all discharges.

The velocity data in the semi-circular flume indicated low velocities in the close vicinity of the semi-circular wetted perimeter, and significantly larger velocities in the bulk of the flow. Typical contour maps of the longitudinal velocity component are presented in Figure 3, at two longitudinal distances x = 2.0 m and x = 7.15 m. At x = 2 m, the velocity distributions were quasi uniform, except next to the wetted perimeter, where some large velocity gradient was recorded next to the invert. At x = 7.15 m further downstream, the velocity profiles became fully-developed, with the maximum longitudinal velocity observed next to the free-surface on the channel centreline, while the velocity gradients next the invert were large along the entire wetted perimeter. Further information on the velocity properties are summarised in Appendix I, including the Boussinesq and Coriolis coefficients, and the ratio of skin friction to total drag. Altogether, the water depth and velocity observations presented findings similar to and consistent with past steady flow measurements in semi-circular channels (Repogle 1964, Kazemipour 1979, Sterling 1998).

The free-surface profiles were analysed to derive the Darcy-Weisbach friction factor of the semi-circular channel based upon energy considerations: i.e. using the best data fit between measured and calculated total head line slopes. The present data are presented in Figure 4 and compared to previous data sets (Kazemipour 1979, Sterling 1998, Chanson 2020). In Figure 4, the Karman-Nikuradse formula for smooth turbulent boundary layer flows is also shown (Liggett 1994, Chanson 2004) (Fig. 4, dashed thick line). Overall, the flow resistance in smooth semi-circular channels was close to, but slightly larger than, that in smooth turbulent flows (Fig. 4). It is believed that the difference accounted for the turbulent dissipation by secondary motion induced by the circular cross-sectional shape.

4. Unsteady flow patterns

Detailed flow visualisations and free-surface measurements were performed for three flow rates Q = 0.015 m^3/s, 0.035 m^3/s and 0.055 m^3/s, corresponding respectively to an initial relative flow depth d_1/D = 0.22, 0.32 and 0.38. For each discharge, different patterns of compression waves were observed within a range of different openings h of the downstream Tainter gate, after closure (Fig. 5). The compression wave properties were detailed at x = 7.15 m (Fig. 5). Figure 5 shows typical photographic observations, from high to low Froude numbers between Figures 5A and 5C. The details of the compression wave properties are reported in the figure caption, including the surge Froude number Fr at x = 7.15 m, defined as:

Accepted manuscript doi:
10.1680/jwama.21.00022

$$Fr = \frac{V_1 + U}{\sqrt{g \times \frac{A_1}{B_1}}} \quad (1)$$

with V_1 the initially-steady cross-sectional velocity, A_1 is the initial cross-section area, B_1 the initial free-surface width and U is the celerity of the compression wave positive upstream. U was estimated from the ultrasonic sensor data.

For a Froude number barely larger than unity, the compression wave was very flat with a pseudo-two-dimensional undular free-surface profile, with some long wave length and small wave amplitude. With an increasing Froude number, the undular compression wave became three-dimensional, with the apparition of lateral cross waves issuing from the sidewalls and intersecting about the channel centreline on the first wave crest (Fig. 5C). The cross-waves continued to propagate downstream across the flume in a pseudo-diamond pattern, in plan view. The cross-wave onset indicated some form of flow separation at the sidewalls (Montes 1986) associated with additional drag (Montes and Chanson 1998). For a further increase in Froude number, the cross-waves became thicker upstream of the first crest, and some breaking occurred at their intersection about the first wave crest, while some smaller cross-waves continued past the first crest (Fig. 5B). The free-surface pattern was three-dimensional with some small secondary waves behind the breaking region. At large Froude numbers, the breaking roller was quasi-two-dimensional, extending over the whole free-surface width (Fig. 5A). The secondary waves disappeared and the roller was very energetic.

The unsteady patterns of the compression wave were systematically observed across all initial flow conditions, although, at low initial flow rates (i.e. $d_1/D < 0.25$), the arrival of the compression wave was associated with a significant change in cross-sectional shape. Herein, the thresholds between patterns differed depending upon the initial relative flow depth d_1/D. For the present experiments, the different compression wave states are shown in Figure 6, with the transition Froude number Fr as a function of the initial relative depth d_1/D. For larger initial discharges (i.e. $d_1/D > 0.35$), the compression wave tended to show more two-dimensional patterns, which were similar to those observed during the propagation of compression waves in rectangular channels (Hornung et al. 1995, Leng and Chanson 2017).

Free-surface measurements were conducted non-intrusively at several longitudinal positions along the channel centreline using the ultrasonic sensors. An ultrasonic sensor is seen in Figure 5C above the surge front. Typical ensemble statistical results are presented in Figure 7 for a breaking surge. Note in Figure 7 that both data sets were recorded with the same initial conditions ($Q = 0.035$ m^3/s, $d_1 = 0.161$ m). In the graph, the blue lines ($Fr = 1.5$) correspond to a complete gate closure and stoppage of the flow. The surge is strong and travel upstream at a celerity $U = 0.91$ m/s. In contrast, the red lines ($Fr = 1.28$) relate to a partial gate closure, resulting in a slower surge celerity ($U = 0.69$ m/s). Thus, the water surface surge time is earlier for $Fr = 1.5$. In Figure 7, the time t is measured from the gate closure, the left axis is the dimensionless ensemble median depth d_{50}/d_1 and the right vertical axis is the difference in quartiles $(d_{75}-d_{25})/d_1$, which characterised the instantaneous free-surface fluctuations. For all experiments and all types of surge, the median depth presented the sudden rise in free-surface elevation during the passage of the compression wave. The compression wave passage induced a sharp increase in water surface fluctuations (Fig. 7). With undular surges, the median depth data showed some pseudo-periodic nature of the secondary undulations, as well as of the free-surface fluctuations (Fig. 7, curve (b), red lines). The trends observed in the present study were qualitatively comparable to observations in rectangular channels (Leng and Chanson 2017), although the current free-surface data highlighted some more

complicated patterns, often with larger free-surface fluctuations, after the compression wave front passage, in the semi-circular channel.

The propagation of a compression wave may be solved using the one-dimensional unsteady open channel flow equations called the Saint Venant equations. Two approach were tested herein: (a) the method of characteristics based upon the simple wave approximation (Henderson 1966, Montes 1998, Chanson 2004), and (b) a numerical integration using the Hartree method (Courant et al. 1952, Montes 1998). The one-dimensional solution was integrated from x = 14 m using the measured initial flow conditions and new discharge after the Tainter gate closure for the downstream boundary condition. Both models gave very close results, since the no friction assumption in the simple wave solution was consistent with the hydraulically smooth flume.

The comparison between the physical observations and the unsteady flow model presented some agreement in terms of the compression wave celerity and height at x = 7.15 m. But the one-dimensional model significantly underestimated the arrival time of the compression wave (Fig. 8). This is illustrated in Figure 8, presenting the measured median water depth and computer depth. The difference was believed to be linked to the compression wave generation process and associated turbulent motion. The unsteady flow model assumed a quasi-instantaneous surge generation, within the physical gate closure time of less than 0.3 s, but the generation of the physical compression wave was a much more complicated and slower three-dimensional physical turbulent process (Sun et al. 2016, Leng 2018). The sudden gate closure induced a water pile-up against the upstream side of the gate, with an overturning motion, followed by a plunging and breaking mechanism after the free-surface overturned, leading to the generation of a breaking roller (Lubin et al. 2010 p. 596, Sun et al. 2016 pp. 91-93, Leng 2018 pp. 105-106). The roller formation lasted a few seconds, before a stable compression wave formed and propagated upstream in a relatively quasi-steady motion. The entire generation process was previously documented though physical and numerical CFD data, for a similar surge generation process with sudden Tainter gate closure (Lubin et al. 2010, Reichstetter 2011, Sun et al. 2016). All previous experimental studies showed a relatively slow generation process. For example, in a 12 m long 0.15 m wide rectangular channel, Reichstetter (2011) observed "*a difference of 7.8 s between the arrivals of the surge front of the simple wave method compared to the physical data*" (p. 48), while Sun et al. (2016) added: "*the generation of the positive surge was a slower process*" (p. 93) in a similar flume.

5. Unsteady velocity data

The upstream propagation of the compression wave caused a sudden flow deceleration as the surge advanced past the velocimeter sampling volume. This was followed by large fluctuations of all velocity components, after a short time lag. Figure 9 shows a typical dimensionless time evolution of ensemble median velocity V_{50} components and instantaneous velocity fluctuation (V_{75}-V_{25}), defined as the difference between the third and first quartile. For a normal distribution of the data set about its mean value, the difference between third and first quartiles (V_{75}-V_{25}) would be equal to 1.3 times the standard deviation of the ensemble.

The longitudinal velocity data showed, at all elevations and for all discharges, a sharp deceleration with the passage of the compression wave. Figure 9A presents a typical example. Further the transverse and vertical velocity data exhibited some sharp fluctuations between the wave passage. Figure 9B shows a typical transverse velocity data set. For all velocity components, large instantaneous velocity fluctuations were observed during and shortly after the compression wave (Fig. 9). In the present study, the data recording stopped

Accepted manuscript doi:
10.1680/jwama.21.00022

when the compression wave reached the upstream end of the channel, to prevent any reflection effect. Thus, the velocity recoding was time-limited and any long-lasting effect, observed in the field (e.g. Chanson et al. 2011, Leng et al. 2018), could not be documented herein.

Although the current measurements were conducted on the channel centreline, the arrival of the compression wave induced a three-dimensional transient response of the velocity field. The response of the flow field to the surge may be analysed as an impulse problem (Lighthill 1978, Kiri et al. 2020). Theoretical considerations would predict large transverse velocities, on both sides, in the shallow-water sections, with an unsteady secondary motion and flow recirculation next to the sides (Fig. 10). Figure 10 presents a solution of the impulse forcing imposed by a sudden longitudinal pressure gradient associated with the passage of a compression wave front in the semi-circular invert profile, with $d_1/D = 0.32$. The invert profile and the initial water depth are also shown in Figure 10. The transverse distribution of the depth-averaged longitudinal velocity was seen to relate to the depth distribution, with recirculation in the shallow waters (Fig. 10). With such a short-lived transient process, the flow pattern would be consistent with the flow separation observed at the inception of cross-waves ahead of the first wave crest.

The Reynolds stress tensor was calculated for the data ensemble. Some typical data are presented in Figure 11 in terms of the normal turbulent stress ($v_x \times v_x$). Figure 11 shows the dimensionless time-variation of the instantaneous median and third quartile of the data ensemble, the latter characterising the instantaneous fluctuation in normal stress. At all elevations and for all flow rates, the turbulent stress data presented a marked increase in instantaneous median Reynolds stress and shear stress fluctuations, during the passage of and shortly after of the compression wave (Fig. 11).

6. Conclusion

The propagation of compression waves in semi-circular channels is a complicated, often three-dimensional transient process. Detailed unsteady experiments in a large laboratory facility regrouped a combination of visual, free-surface and velocity measurements in a semi-circular channel. The free-surface observations indicated some complicated three-dimensional features, with cross-waves and surface breaking for a range of Froude numbers. At higher Froude number, the compression wave was quasi-two-dimensional with a breaking roller expanding across the entire channel width. The ensemble statistics of free-surface and velocity measurements demonstrated the marked impacts of the compression wave passage. These included a sharp increase in water elevation and streamwise deceleration. The former may explain the explosive incidents reported in some urban waterways. Further seminal features encompassed some large transient instantaneous fluctuations in terms of water depth, velocity components and Reynolds stresses.

Further analyses hinted that the semi-circular channel shape tended to induce larger instantaneous fluctuations than observations of positive surges in rectangular channels. Future research would include unsteady velocity measurements across the whole cross-section, to characterise sidewall effects, including recirculation and secondary currents.

Acknowledgements

The authors thank the reviewees for helpful and constructive suggestions. They further acknowledge the technical assistance of Jason Van Der Gevel and Stewart Matthews (The University of Queensland, Australia) and the financial assistance of the School of Civil Engineering at The University of Queensland (Australia). HC thanks Dr Daniel Valero for sharing the information on the Arrudas River incident.

Accepted manuscript doi:
10.1680/jwama.21.00022

Appendix I - Key summary of velocity properties in semi-circular channel (present data)

Detailed steady flow measurements were conducted at two locations x = 2 m and 7.15 m in the semi-circular channel. The velocity data were analysed to derive the momentum correction coefficient β, or Boussinesq coefficient, and the kinetic energy correction coefficient α, or Coriolis coefficient. Further the skin friction boundary shear stress was recorded along the entire wetted perimeter, using the Prandlt-Pitot tube acting as Preston tube, based upon the detailed calibration of the tube by Cabonce et al. (2019), and the data were integrated, yielding the relative skin friction f_{skin}/f. The data are summarised below.

Property	Units	Q = 0.035	m^3/s	Q = 0.08	m^3/s
		x = 2.0 m	x = 7.15 m	x = 2.0 m	x = 7.15 m
V_{mean}	m/s	0.656	0.709	0.798	0.884
d	m	0.168	0.160	0.236	0.230
A	m^2	0.0579	0.0542	0.091	0.088
P_w	m	0.618	0.601	0.758	0.745
β	-	1.051	1.096	1.061	1.072
α	-	1.128	1.169	1.112	1.105
f_{skin}/f	-	0.781	0.639	0.897	0.602

List of notations

A is the cross-sectional area

B is the free-surface width

D is the internal pipe diameter

D_H is the hydraulic diameter

d is the water depth measured above the lowest invert elevation

d_1 is the initial steady flow depth measured above the lowest invert elevation

d_c is the critical flow depth

Fr is the Froude number of the compression wave, defined as $Fr = (V_1+U)/(g\times A_1/B_1)^{1/2}$

f is the Darcy-Weisbach friction factor

f_{skin} is the dimensionless skin friction boundary shear stress expressed in the form of a friction factor

g is the gravity acceleration

h is the tainter gate opening after closure

Q is the initial steady flow discharge

P_w is the wetted perimeter

R is the internal pipe radius: R = D/2

Re is the Reynolds number defined in terms of the hydraulic diameter: $Re = \rho\times V\times D_H/\mu$

S_o is the longitudinal bed slope

t is the time

U is the compression wave celerity

V is the velocity

V_1 is the initial steady flow cross-sectional averaged velocity

V_x is the instantaneous longitudinal velocity component

V_y is the instantaneous transverse velocity component

V_z is the instantaneous vertical velocity component

v is the velocity fluctuation

v_x is the instantaneous longitudinal velocity fluctuation

v_y is the instantaneous transverse velocity fluctuation

v_z is the instantaneous vertical velocity fluctuation

x is the longitudinal co-ordinate positive downstream

y is the transverse co-ordinate

z is the vertical co-ordinate positive upwards

α is the kinetic energy correction coefficient

β is the momentum correction coefficient

μ is the water dynamic viscosity

ρ is the water density

Subscript

c is the critical flow condition

1 initial flow conditions

25 is the first quartile

50 is the median

75 is the third quartile

References

Cabonce, J., Fernando, R., Wang, H., and Chanson, H. (2019). Using Small Triangular Baffles to Facilitate Upstream Fish Passage in Standard Box Culverts. Environmental Fluid Mechanics, Vol. 19, No. 1, pp. 157–179 (DOI: 10.1007/s10652-018-9604-x).

Capart, H., Sillen, X., and Zech, Y. (1997). Numerical and experimental water transients in sewer pipes. Journal of Hydraulic Research, IAHR, Vol. 35, No. 5, pp. 659-672.

Chanson, H. (2004). *Environmental Hydraulics of Open Channel Flows*. Elsevier-Butterworth-Heinemann, Oxford, UK, 483 pages.

Chanson, H. (2020). Low Velocity Zone in Smooth Pipe Culvert with and without Streamwise Rib for Fish Passage. Journal of Hydraulic Engineering, ASCE, Vol. 146, No. 9, Paper 04020059, 10 pages (DOI: 10.1061/(ASCE)HY.1943-7900.0001789).

Chanson, H., Reungoat, D., Simon, B., and Lubin, P. (2011). High-Frequency Turbulence and Suspended Sediment Concentration Measurements in the Garonne River Tidal Bore. Estuarine Coastal and Shelf Science, Vol. 95, No. 2-3, pp. 298-306 (DOI 10.1016/j.ecss.2011.09.012).

Courant, R., Isaacson, E., and Rees, M. (1952). On the solution of nonlinear hyperbolic differential equations by finite differences. Commun. Pure Appl. Math., Vol. 5, No. 3, pp. 243-255.

Cunge, J.A., and Wegner, M. (1964). Intégration Numérique des Equations d'Ecoulement de Barré de Saint Venant par une Schéma Implicite de Différences Finies. (' Numerical Integration of Barré de Saint Venant's Flow Equations by Means of an Implicit Scheme of Finite Differences.') Jl La Houille Blanche, No. 1, pp. 33-39 (in French).

Favre, H. (1935). Etude Théorique et Expérimentale des Ondes de Translation dans les Canaux Découverts. ('Theoretical and Experimental Study of Travelling Surges in Open Channels.') Dunod, Paris, France (in French).

Furgerot, L., Mouaze, D., Tessier, B., Perez, L., Haquin, S., Weill, P., and Crave, A. (2016). Sediment transport induced by tidal bores. An estimation from suspended matter measurements in the Sée River (Mont-Saint-Michel Bay, northwestern France). Comptes Rendus Géoscience, Vol. 348, pp. 432-441 (DOI: 10.1016/j.crte.2015.09.004).

Hager, W.H. (1999). *Wastewater Hydraulics*. Springer- Verlag, Berlin, Germany, 628 pages.

Henderson, F.M. (1966). *Open Channel Flow*. MacMillan Company, New York, USA.

Hornung, H.G., Willert, C., and Turner, S. (1995). The Flow Field Downstream of a Hydraulic Jump. Journal of Fluid Mechanics, Vol. 287, pp. 299-316.

Kazemipour, A.K. (1979). Cross-sectional Shape effects on Resistance to Uniform Flow in Open Channels and Non-circular Closed Conduits. Ph.D. thesis, The University of Queensland, Department of Civil Engineering, Brisbane, Australia, 462 pages.

Khezri, N., and Chanson, H. (2012). Sediment Inception under Breaking Tidal Bores. Mechanics Research Communications, Vol. 41, pp. 49-53 & 1 video movie (DOI 10.1016/j.mechrescom.2012.02.010).

Kiri, U., Leng, X., and Chanson, H. (2020). Transient Secondary Currents behind a Compression Wave in an Irregular Channel. Environmental Fluid Mechanics, Vol. 20, No. 4, pp. 1053-1073 & 1 vide movie (DOI: 10.1007/s10652-020-09740-y).

Leng, X. (2018). A Study of Turbulence: the Unsteady Propagation of Bores and Surges. Ph.D. thesis, School of Civil Engineering, The University of Queensland, Brisbane, Australia, 364 pages & 2 Digital Appendices (DOI: 10.14264/uql.2018.501).

Leng, X., and Chanson, H. (2017). Upstream Propagation of Surges and Bores: Free-Surface Observations. Coastal Engineering Journal, Vol. 59, No. 1, paper 1750003, 32 pages & 4 videos (DOI: 10.1142/S0578563417500036).

Leng, X., Chanson, H., and Reungoat, D. (2018). Turbulence and Turbulent Flux Events in Tidal Bores: Case Study of the Undular Tidal Bore of the Garonne River. Environmental Fluid Mechanics, Vol. 18, No. 4, pp. 807-828 (DOI: 10.1007/s10652-017-9561-9).

Liggett, J.A. (1994). *Fluid Mechanics*. McGraw-Hill, New York, USA.

Lighthill, J. (1978). *Waves in Fluids*. Cambridge University Press, Cambridge, UK, 504 pages.

Lubin, P., Chanson, H., and Glockner, S. (2010). Large Eddy Simulation of Turbulence Generated by a Weak Breaking Tidal Bore. Environmental Fluid Mechanics, Vol. 10, No. 5, pp. 587-602 (DOI: 10.1007/s10652-009-9165-0)

Montes, J.S. (1986). A Study of the Undular Jump Profile. Proc. 9th Australasian Fluid Mechanics Conference AFMC, Auckland, New Zealand, pp. 148-151.

Montes, J.S. (1998). *Hydraulics of Open Channel Flow*. ASCE Press, New-York, USA, 697 pages.

Montes, J.S., and Chanson, H. (1998). Characteristics of Undular Hydraulic Jumps. Results and Calculations. Journal of Hydraulic Engineering, ASCE, Vol. 124, No. 2, pp. 192-205 (DOI: 10.1061/(ASCE)0733-9429(1998)124:2(192)).

Pozos-Estrada, O., Pothof, I., Fuentes-Mariles, O,A., Dominguez-Mora, R., Pedrozo-Acuna, A., Meli, R., and Pena, F. (2015). Failure of a drainage tunnel caused by an entrapped air pocket. Urban Water Journal, Vol. 12, No. 6, pp. 446-454 (DOI: 10.1080/1573062X.2015.1041990).

Reichstetter. (2011). Hydraulic Modelling of Unsteady Open Channel Flow: Physical and Analytical Validation of Numerical Models of Positive and Negative Surges. MPhil thesis, School of Civil Engineering, The University of Queensland, Brisbane, Australia, 112 pages.

Repogle, J.A. (1964). Tractive-Force Distribution in Sewers and Channels. Ph.D. thesis, University of Illinois, USA, 256 pages.

Repogle, J.A., and Chow, V.T. (1966). Tractive-Force Distribution in Open Channels. Journal of Hydraulic Division, ASCE, Vol. 92, No. HY2, pp. 169-191.

Song, C.C.S., Cardle, J.A., and Leung, K.S. (1983). Transient Mixed-Flow Models for Storm Sewers. Journal of Hydraulic Engineering, ASCE, Vol. 109, No. 11, pp. 1487-1504.

Sterling, M. (1998). A study of boundary shear stress, flow resistance and the free overfall in open channels with a circular cross section. PhD thesis, University of Birmingham, School of Civil Engineering, Birmingham, U.K., 541 pages.

Sterling, M., and Knight, D.W. (2000). Resistance and boundary shear in circular conduits with flat beds running part full. Proceedings of the Institution of Civil Engineers, Water & Maritime Engineering, UK, Vol. 142, pp. 229-240.

Sun, S., Leng, X., and Chanson, H. (2016). Rapid Operation of a Tainter Gate: Generation Process and Initial Upstream Surge Motion. Environmental Fluid Mechanics, Vol. 16, No. 1, pp. 87-100 (DOI: 10.1007/s10652-015-9414-3).

Treske, A. (1994). Undular Bores (Favre-Waves) in Open Channels - Experimental Studies. Journal of Hydraulic Research, IAHR, Vol. 32, No. 3, pp. 355-370. Discussion: Vol. 33, No. 3, pp. 274-278.

Table 1 Properties at x = 7.15 m of steady flow conditions

Q	d	V	Re	A	B	P_w	f
m^3/s	m	m/s		m^2	m	m	
0.080	0.228	0.917	1.2×10^5	0.08718	0.498	0.7413	0.016
0.055	0.191	0.798	0.93×10^5	0.06895	0.4858	0.6662	0.021
0.035	0.161	0.641	0.65×10^5	0.05463	0.4672	0.6034	0.0216
0.015	0.1085	0.477	3.5×10^4	0.0314	0.4122	0.4845	0.030
0.008	0.0875	0.347	2.1×10^4	0.02307	0.3799	0.4316	0.038
0.005	0.057	0.404	1.6×10^4	0.01238	0.3178	0.3444	0.0205

Table 2 Properties at x = 7.15 m of unsteady compression wave experiments

Q	d_1	V_1	U	Fr	h
m^3/s	m	m/s	m/s		m
0.055	0.191	0.797	0.803	1.567	0
			0.976	1.554	0.01
			0.901	1.488	0.02
			0.847	1.441	0.03
			0.837	1.432	0.04
			0.788	1.389	0.05
			0.746	1.352	0.06
			0.73	1.338	0.07
			0.666	1.282	0.08
0.035	0.161	0.64	0.909	1.496	0
			0.871	1.459	0.01
			0.81	1.401	0.02
			0.702	1.295	0.03
			0.691	1.285	0.04
			0.69	1.284	0.05
			0.636	1.232	0.06
			0.598	1.196	0.07
			0.564	1.163	0.08
0.015	0.109	0.477	0.68	1.384	0
			0.692	1.398	0.01
			0.651	1.35	0.02
			0.562	1.243	0.03
			0.519	1.192	0.04
			0.463	1.125	0.05
			0.417	1.069	0.06
			0.377	1.022	0.07
			0.359	1	0.08

Accepted manuscript doi:
10.1680/jwama.21.00022

Figure captions

Figure 1. Circular conduits. (A) Pipe culvert outlet in Brisbane on 9 February 2020; (B) Dimensionless relationships between the free-surface width B, cross-section area A, wetted perimeter P_w, hydraulic diameter D_H and water depth d; (C) Definition sketch

Figure 2. Photograph of the experimental channel for Q = 0.015 m^3/s, looking downstream

Figure 3. Contour maps of longitudinal velocity in semi-circular channel with D = 0.50 m, S_o = 0 for Q = 0.035 m^3/s at (A) x = 2 m and (B) x = 7.15 m

Figure 4. Flow resistance in smooth semi-circular channels: Darcy-Weisbach friction factor at a function of the Reynolds number - Comparison between current and previous data sets (Kazemipour 1979, Sterling 1998, Chanson 2020), as well as smooth turbulent flow (Karman-Nikuradse formula)

Figure 5. Basic observations of compression waves propagating in semi-circular channel (D = 0.5 m). (A) Two-dimensional breaking bore, looking downstream at incoming bore roller - Q = 0.035 m^3/s, x = 7.15 m, d_1 = 0.161 m, U = 0.91 m/s, Fr = 1.5, (B) Breaking bore with secondary undulations, with 0.3 s between each photograph - Q = 0.015 m^3/s, x = 7.15 m, d_1 = 0.109 m, U = 0.68 m/s, Fr = 1.38, (C) Undular surge with relatively weak cross-waves intersecting on the channel centreline about the first wave crest - Q = 0.055 m^3/s, x = 7.15 m, d_1 = 0.191 m, U = 0.67 m/s, Fr = 1.28 - Left: three-quarter view; Right: looking downstream at incoming compression wave

Figure 6. Dimensionless chart of the different compression wave states in a semi-circular channel: transition Froude number Fr as a function of the initial relative depth d_1/D

Figure 7. Dimensionless time variations of ensemble median water elevation d_{50} and quartile difference (d_{75}-d_{25}) of compression waves propagating upstream in semi-circular channel for two flow conditions: (a, blue lines) Q = 0.035 m^3/s, x = 7.15 m, d_1 = 0.161 m, Fr = 1.5 (h = 0); U = 0.91 m/s; breaking bore (b, red lines) Q = 0.035 m^3/s, x = 7.15 m, d_1 = 0.161 m, Fr = 1.28 (h = 0.050 m); U = 0.69 m/s, undular bore

Figure 8. Dimensionless time variations of water elevation during compression wave propagation in a semi-circular channel: comparison between present experimental data (ensemble-median of 25 repeats) and unsteady flow model based upon the Saint Venant equations (SVE) for two conditions

Figure 9. Dimensionless time variations of ensemble median longitudinal velocity V_x and transverse velocity V_y, and quartile differences, during the upstream propagation of compression wave in semi-circular channel - Q = 0.035 m^3/s, x = 7.15 m, d_1 = 0.161 m, V_1 = 0.64 m/s, U = 0.70 m/s, Fr = 1.44, z = 0.140 m - (A) V_x data; (B) V_y data

Figure 10. Transverse distribution of dimensionless longitudinal velocity V/V_1 for an impulse forcing imposed by a longitudinal pressure gradient during the passage of a compression wave in a channel with a semi-circular channel with d_1/D = 0.32

Figure 11. Dimensionless time variations of ensemble median normal stress (v_x.v_x) and third quartile during the upstream propagation of compression wave in semi-circular channel - Q = 0.035 m^3/s, x = 7.15 m, d_1 = 0.161 m, V_1 = 0.64 m/s, V_1 = 0.64 m/s, U = 0.70 m/s, Fr = 1.44, z = 0.140 m

Accepted manuscript doi:
10.1680/jwama.21.00022

F01A_IMG_20200209_061359981c

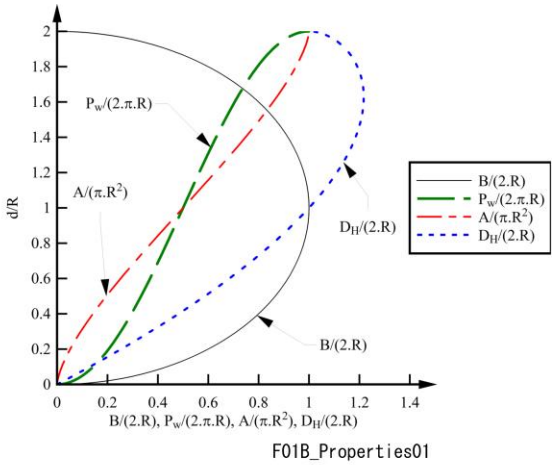

F01B_Properties01

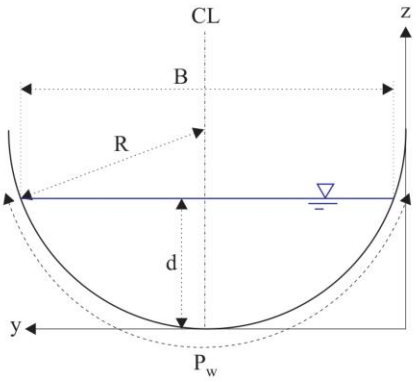

F01C_Circ_channel_02

Accepted manuscript doi:
10.1680/jwama.21.00022

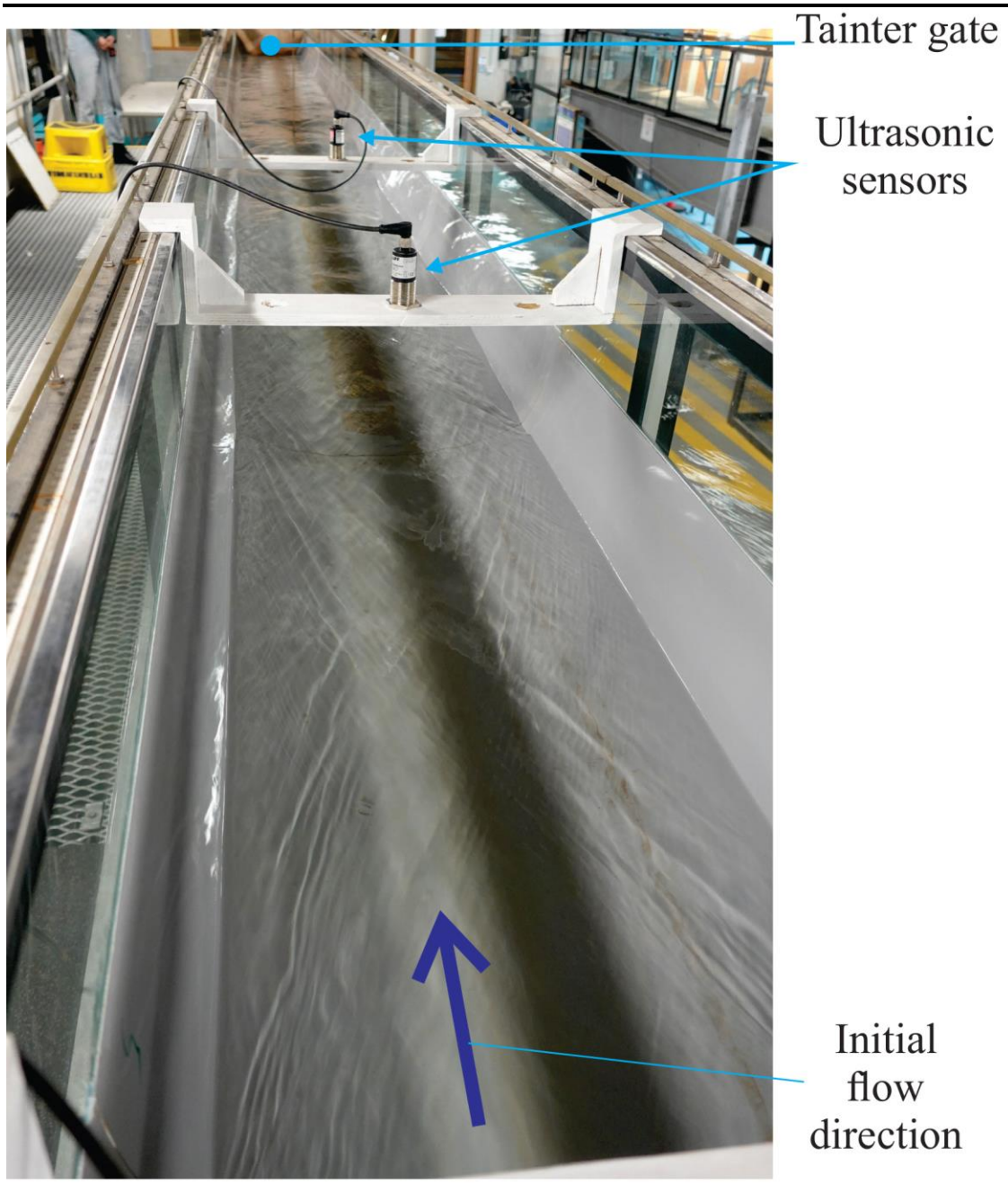

F02_DSC00372

Accepted manuscript doi:
10.1680/jwama.21.00022

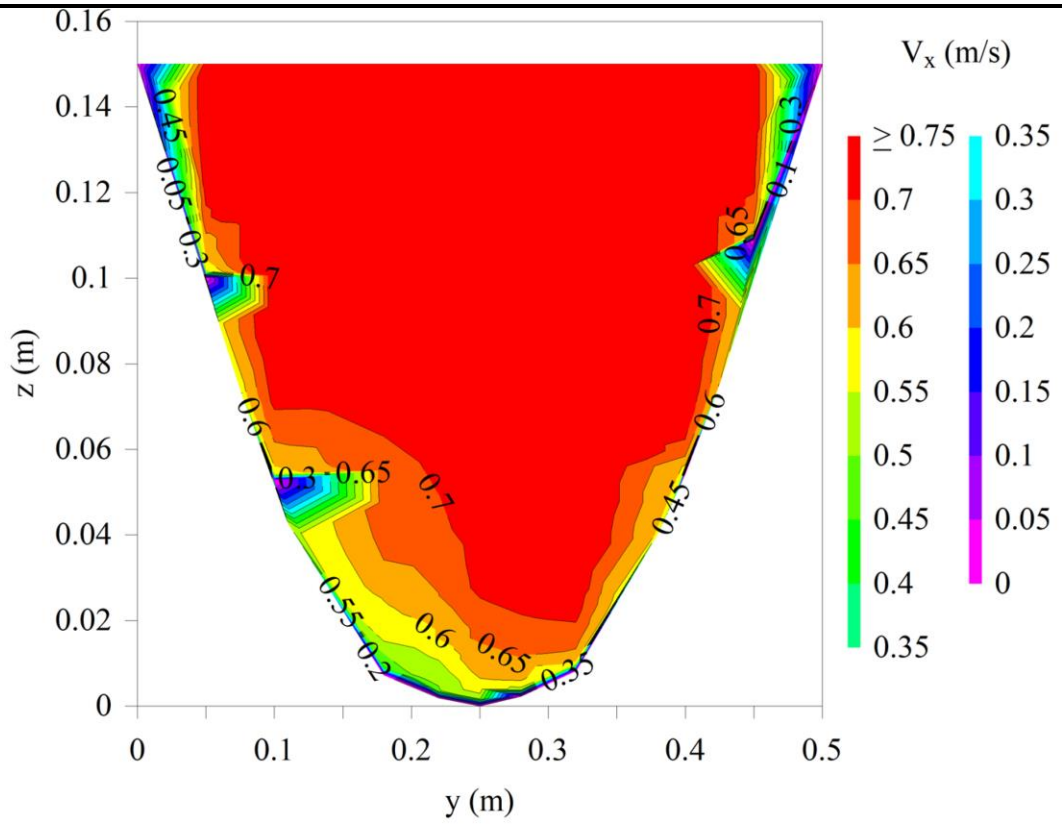

F03A_Contour 35lps x=2M UPDATED

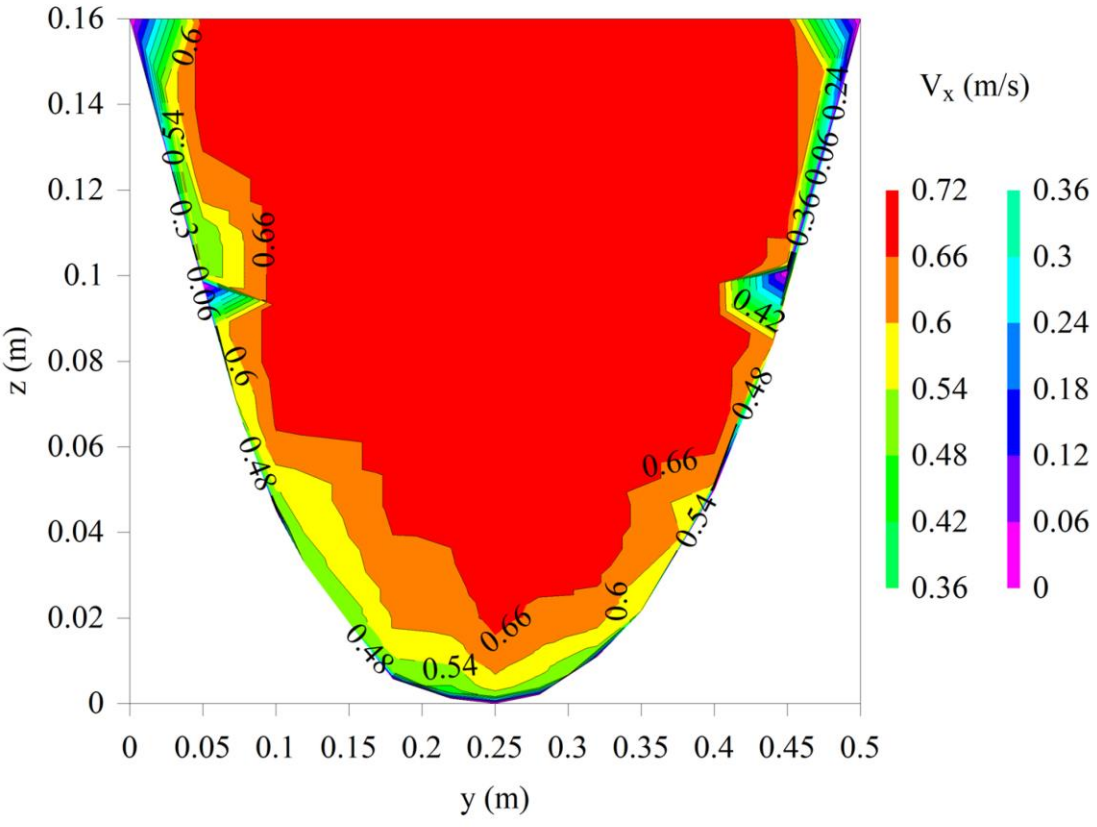

F03B_Contour 35lps x=7.15m UPDATED

Accepted manuscript doi:
10.1680/jwama.21.00022

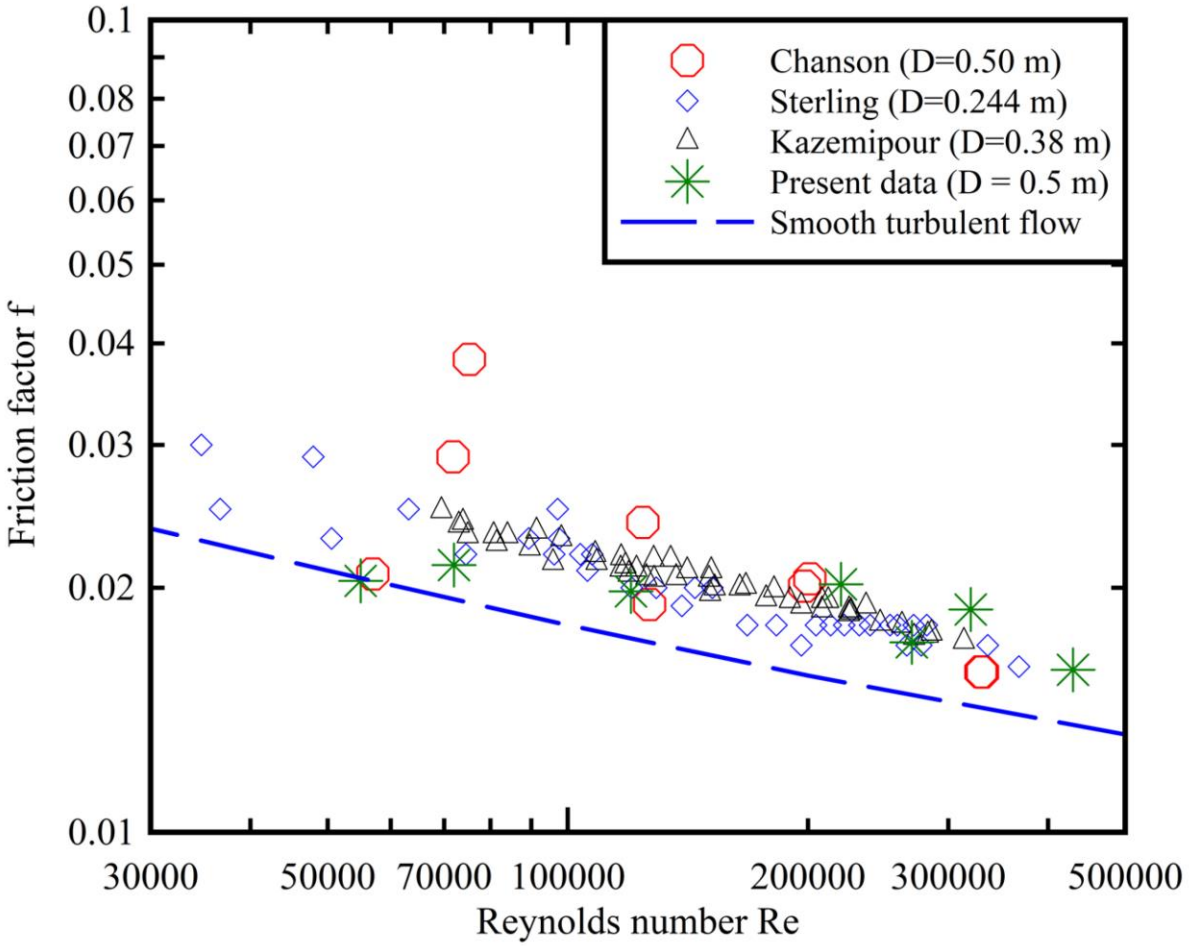

F04_f_Re_04c

Accepted manuscript doi:
10.1680/jwama.21.00022

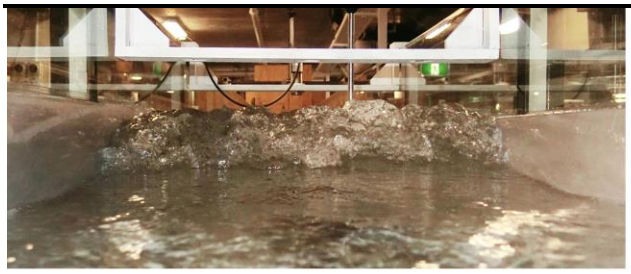

F05A_CIMG7364c

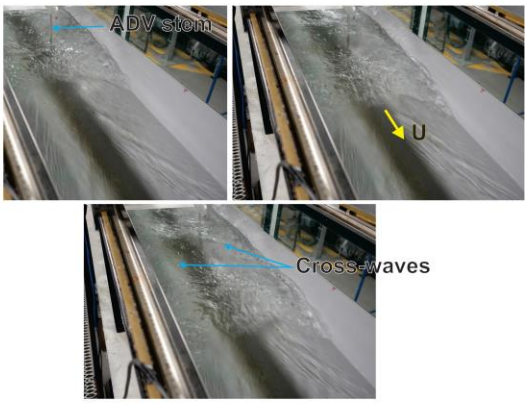

F05B_DSC00816

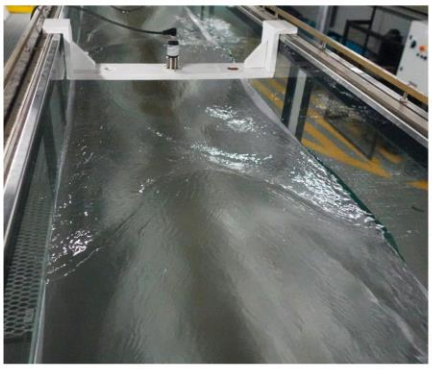

F05C_Left_DSC00142c

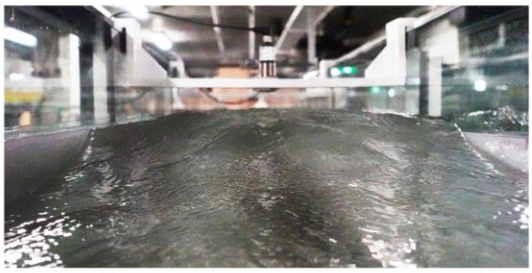

F05C_Right_DSC00203c

Accepted manuscript doi:
10.1680/jwama.21.00022

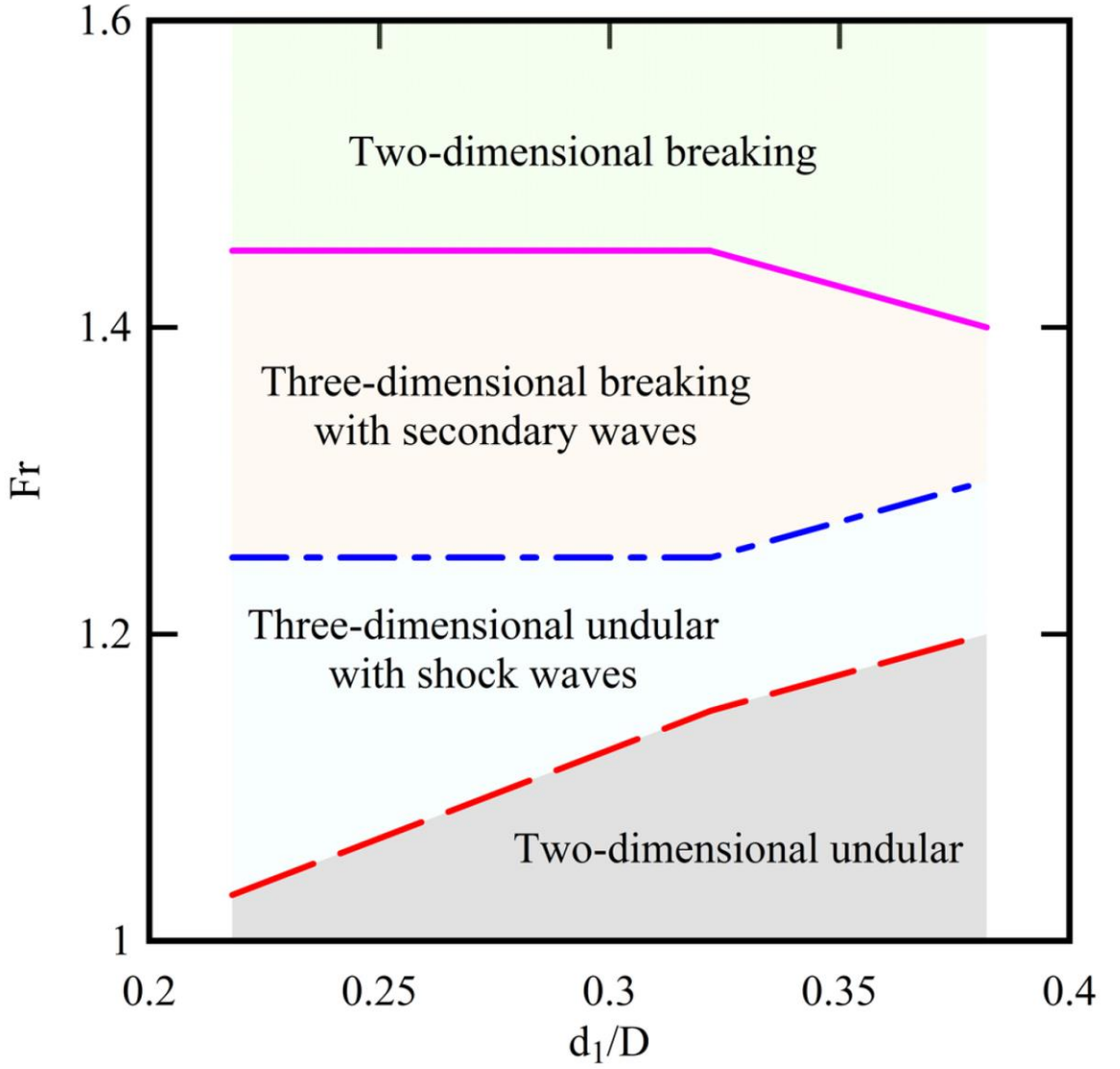

F06_UnsteadyFlowRegime

Accepted manuscript doi:
10.1680/jwama.21.00022

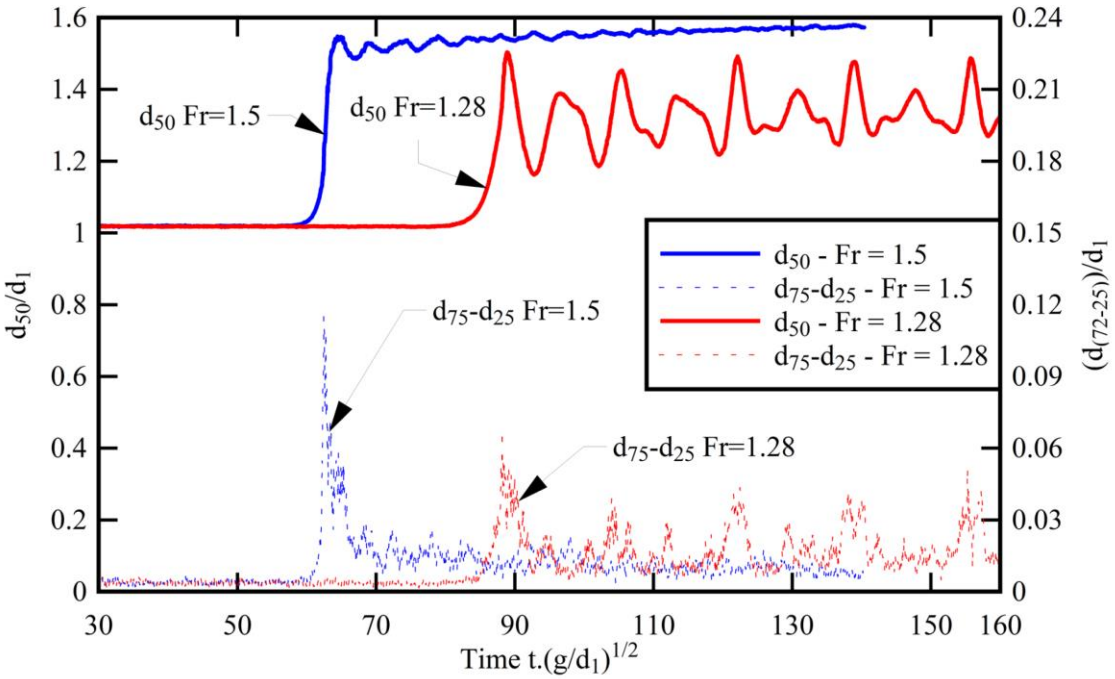

F07_Q35_mean_difference_quartile for 3

Accepted manuscript doi:
10.1680/jwama.21.00022

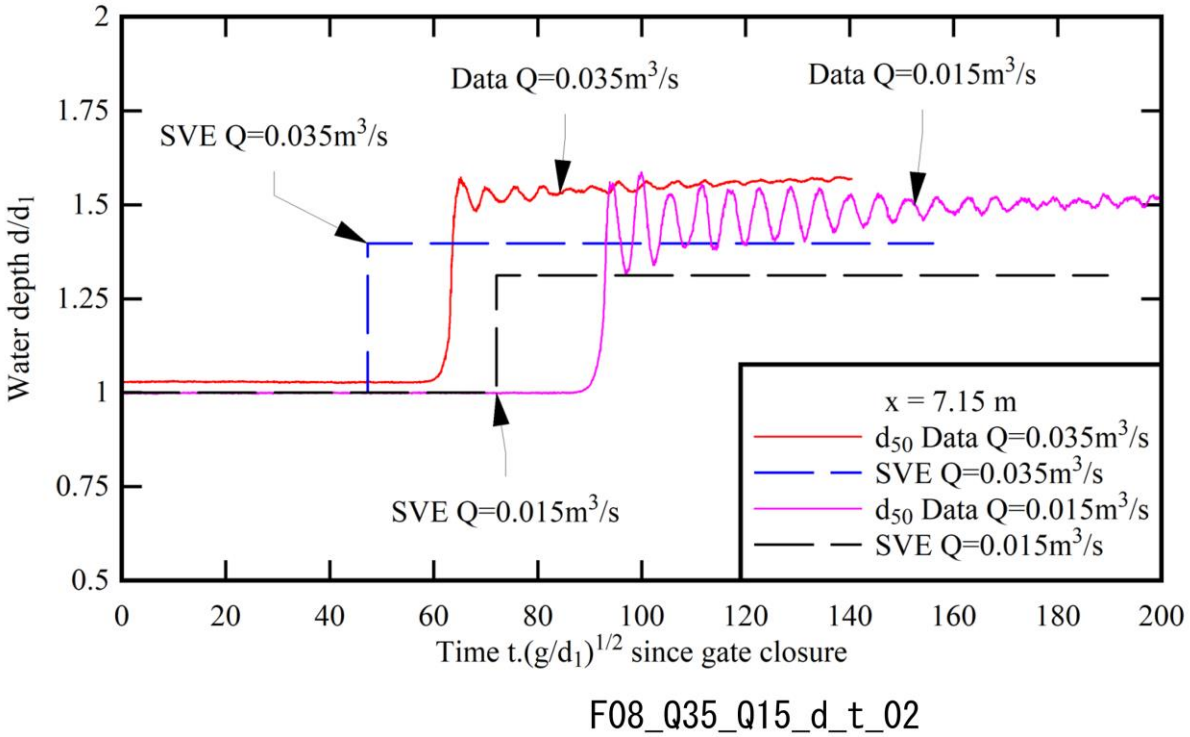

F08_Q35_Q15_d_t_02

Accepted manuscript doi:
10.1680/jwama.21.00022

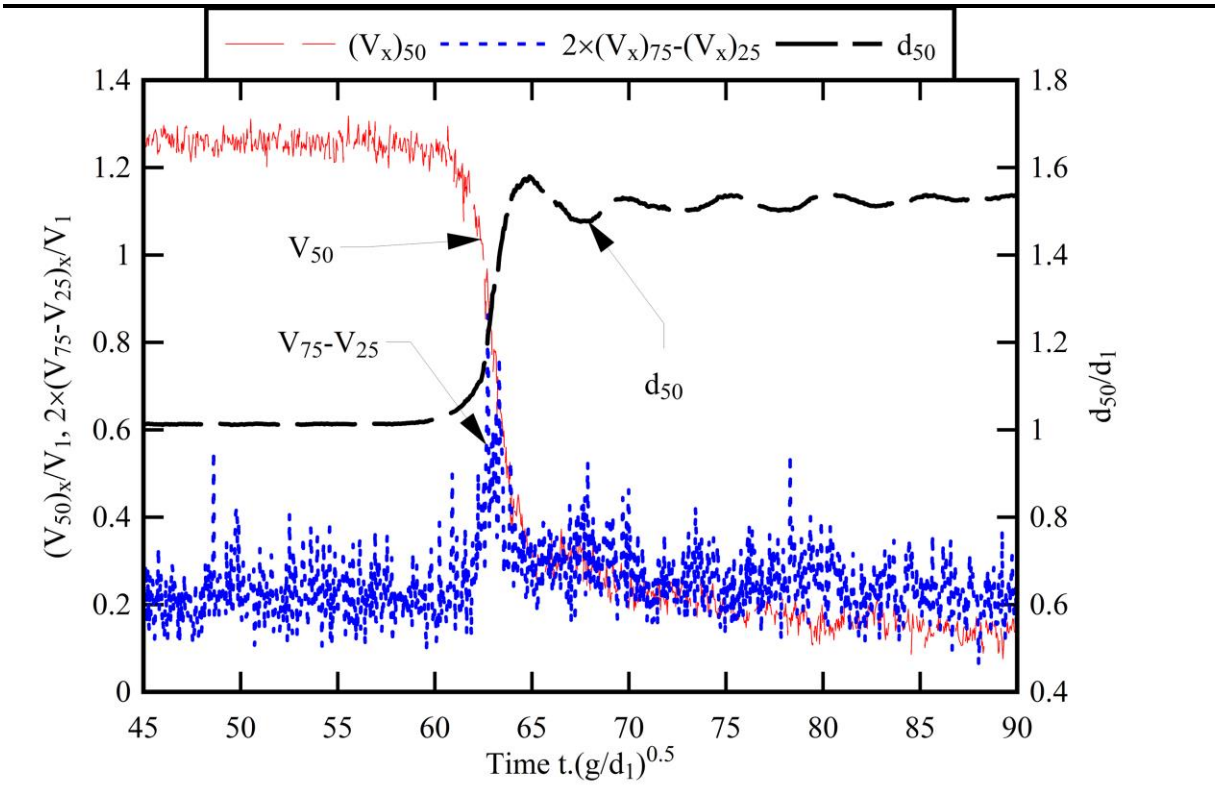

F09A_Vx_Q35_140mmelevation_25runs_0

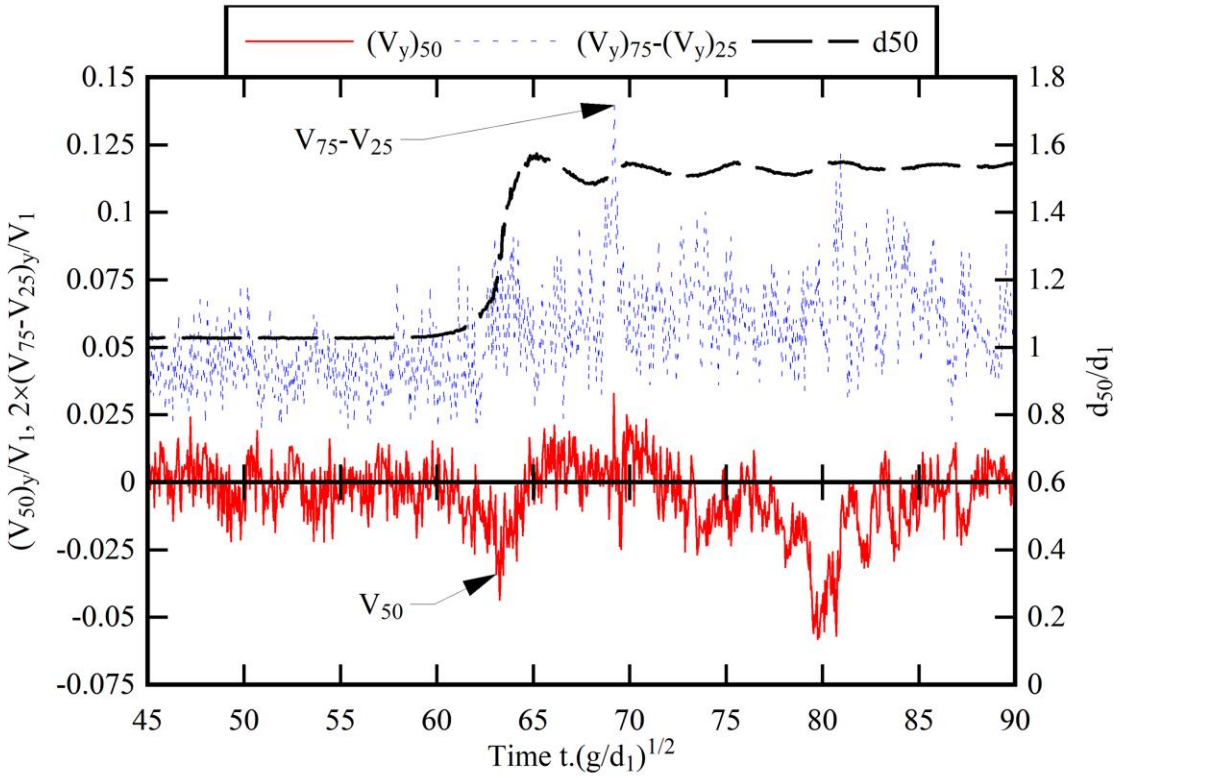

F09B_Vy_Q35_140mmelevation_25runs

Accepted manuscript doi:
10.1680/jwama.21.00022

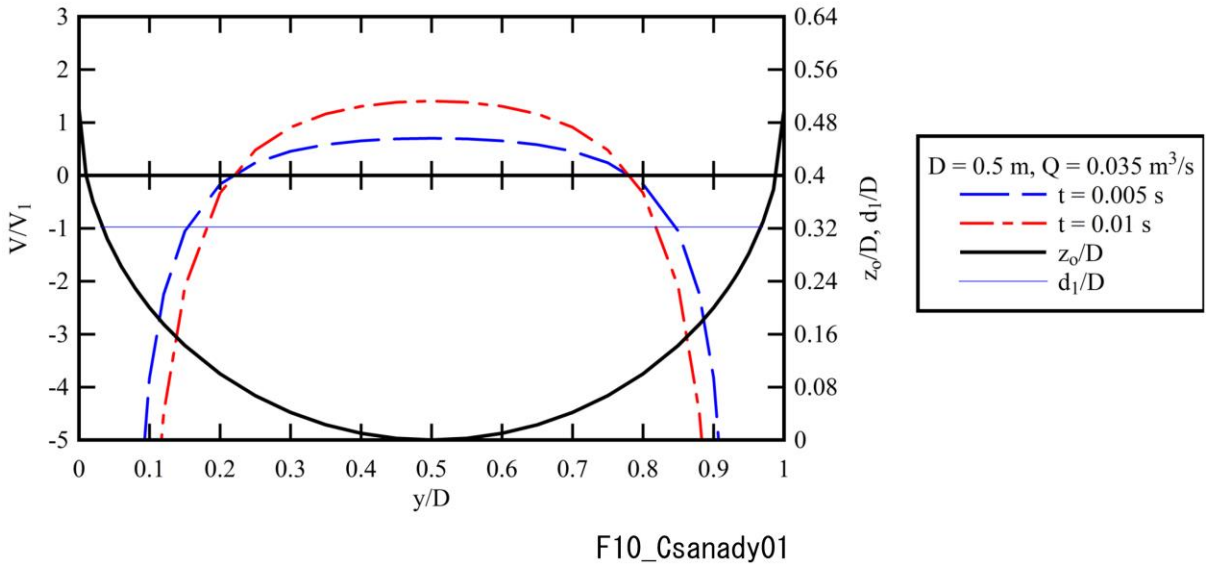

F10_Csanady01

Accepted manuscript doi:
10.1680/jwama.21.00022

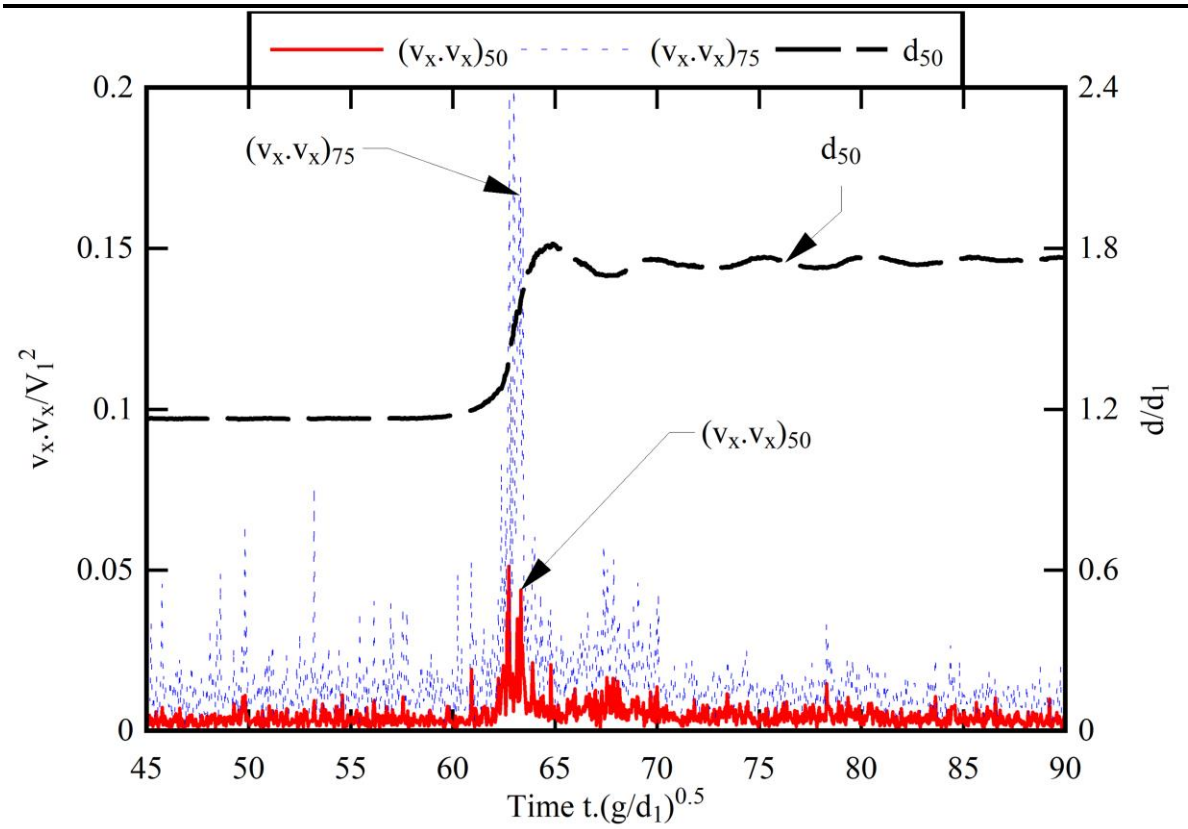

F11_Reynolds_(vx.vx)_35lps_140mm